

Thickness and composition effects on atomic moments and magnetic compensation point in rare-earth transition-metal thin films

Daniel H. Suzuki ¹, Manuel Valvidares ², Pierluigi Gargiani,² Mantao Huang,¹
Alexander E. Kossak ¹ and Geoffrey S. D. Beach^{1,*}

¹*Department of Materials Science and Engineering, Massachusetts Institute of Technology, Cambridge, Massachusetts 02139, USA*

²*ALBA Synchrotron Light Source, Barcelona E-08290, Spain*



(Received 19 September 2022; revised 21 February 2023; accepted 10 April 2023; published 21 April 2023)

Rare-earth (RE) transition-metal (TM) thin films have exhibited great promise for spintronic applications; however, the variation of their magnetic properties with composition and thickness has yet to be adequately quantified. In this paper, we investigate the atomic magnetic moments of few-nanometer-thick GdCo and TbCo via x-ray magnetic circular dichroism and find a significant decrease in both RE and Co average moments with increasing RE concentration, consistent with a local Co environment model description. We observe a shift in compensation composition to higher RE concentrations as the thickness of GdCo and TbCo films decreases <10 nm. Based on the dependence of the saturation magnetization (M_s) on temperature and thickness, we posit the existence of an intrinsic unalloyed RE dead layer at room temperature that reduces the effective RE concentration in the remaining alloyed region, resulting in significant, nonzero M_s in thin films at higher RE concentrations than is observed in thick films. We demonstrate a simple model for RE-TM films that accurately describes M_s as a function of both RE content and film thickness. In addition, the atomic g factors of GdCo and TbCo are found to vary significantly with RE concentration, largely deviating from their elemental values over the bulk of composition space.

DOI: [10.1103/PhysRevB.107.134430](https://doi.org/10.1103/PhysRevB.107.134430)

I. INTRODUCTION

Rare-earth (RE) transition-metal (TM) amorphous alloys have regained prominence in recent years due to their utility in spintronic devices. Spin-transport phenomena such as ultrafast domain wall motion [1–4], stable room-temperature skyrmion generation [2,5], all-optical switching [6,7], and field-free spin-orbit torque switching [8,9] have all been observed in RE-TM heterostructures, facilitated by their unique properties. Many of these properties are due to the antiferromagnetic coupling between the RE and TM sublattices, resulting in net ferrimagnetic behavior. The ferrimagnetic nature of RE-TM alloys means that their magnetization and net spin can be tuned by varying the temperature (T) and the compositions of the RE and TM sublattices, allowing for fine control of a variety of dependent magnetic properties such as anisotropy and compensation temperatures, with critical consequences on static and dynamic behavior.

Generally, RE-TM alloys are modeled as a pair of antiferromagnetically coupled sublattices such that the net saturation magnetization is given by $M_s = |M_{\text{RE}} - M_{\text{TM}}|$. This model allows one to estimate net properties such as the effective g factor of the material or the T -dependent saturation magnetization [10,11]. In practice, the sublattice magnetizations are not known individually, or their values are assumed based on the pure elemental magnetizations scaled by their volume fractions in the alloy.

In this paper, we investigate the variation of magnetic moments in GdCo and TbCo as a function of RE composition (x) and thickness (t). We find that the compensation composition undergoes a systematic shift to higher RE concentrations with decreasing t as the RE-TM film drops <10 nm. We use x-ray magnetic circular dichroism (XMCD) to probe the atomic magnetic properties of each element independently as a function of x and observe a clear decrease in both RE and TM moments with increasing x at room temperature. We additionally observe a significant variation in atomic g factors as a function of x . Finally, we model M_s as a function of t and x for RE-TM alloys by inclusion of a RE dead layer that shifts the compensation composition of thin films.

II. EXPERIMENTAL METHODS

Films of Ta(4)/Pt(4)/Gd _{x} Co_{1- x} (t)/Ta(4)/Pt(2) and Ta(4)/Pt(4)//Tb _{x} Co_{1- x} (6)/Ta(3)//Ta(3)/Pt(2) were grown by DC magnetron sputtering [numbers in parenthesis are thickness in nanometers, and x is the RE atomic fraction; see Fig. 1(a)] on thermally oxidized Si wafers with $x = 0-0.7$ and $t = 3$ and 6 nm. The TbCo films were grown in three steps (with vacuum breaks indicated by double slashes) due to a sputter gun limitation. The GdCo and TbCo layers were grown by cosputtering Gd or Tb with Co. An Ar pressure of 3 mTorr with a background pressure $<2 \times 10^{-7}$ Torr was used during deposition. Layer thicknesses and nominal alloy atomic fractions were determined from sputtering rates calibrated using x-ray reflectometry. The atomic compositions of RE-Co layers were calculated using the ratio of the RE and Co deposition rates normalized by their

*gbeach@mit.edu

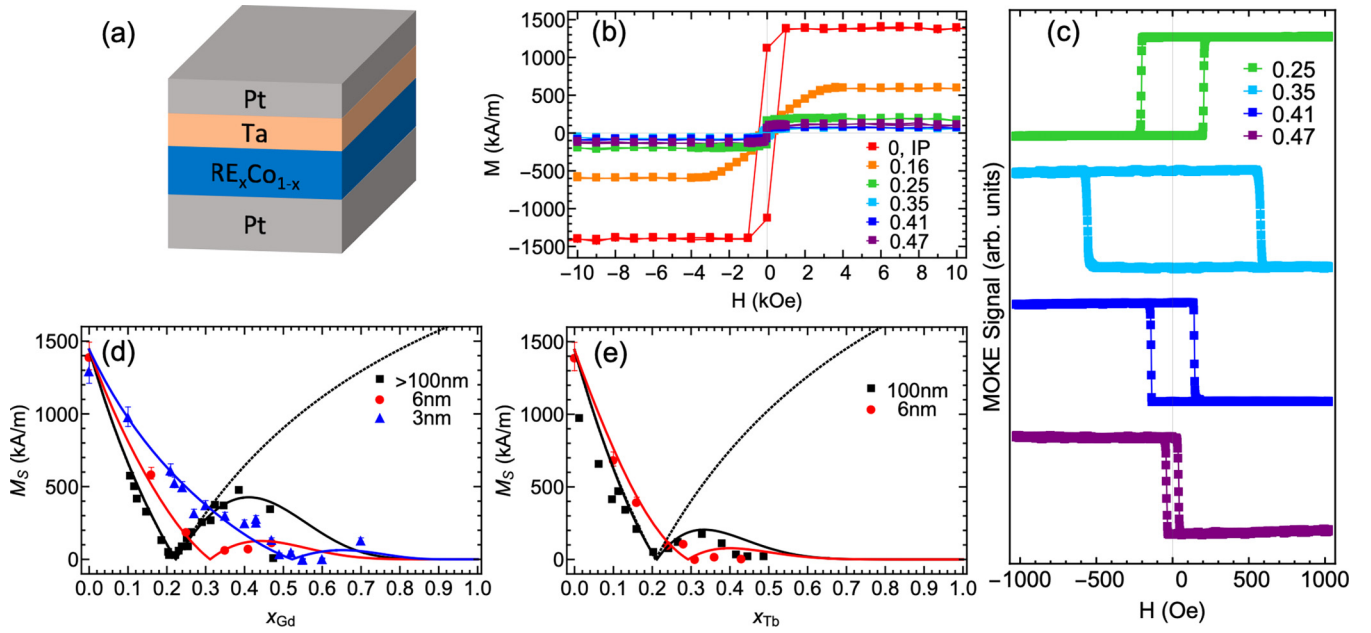


FIG. 1. Vibrating sample magnetometer and magneto-optical Kerr effect (MOKE) data of GdCo and TbCo films. (a) Layer structure of rare-earth (RE)-Co films grown by sputter deposition. (b) Vibrating sample magnetometer hysteresis loops of 6-nm GdCo films used to determine saturation magnetization M_s . All loops were measured in an out-of-plane configuration except for pure Co (red). The legend refers to Gd atomic fraction. (c) MOKE loops of 6-nm GdCo with perpendicular magnetic anisotropy. Right-facing loop (green) is Co dominant, and left-facing loops (cyan, blue, and purple) are Gd dominated. (d) GdCo M_s data at room temperature. Solid curves are based on a combined environment plus Gd dead layer model (see text). Dotted line is the predicted M_s assuming constant atomic Gd and Co moments across composition. Black squares are from Ref. [14]. (e) TbCo M_s data at room temperature. Black squares are from Ref. [28].

molar masses and bulk densities with $\sim 1\%$ uncertainty. The compositions were controlled by controlling the RE gun current to tune the RE deposition rate relative to the Co rate. The bottom Pt layer of the films was chosen to replicate the Pt/GdCo multilayers used for current-induced domain wall motion and room-temperature magnetic skyrmion generation [2–4,12]. The top Ta/Pt layer was added to prevent sample oxidation. For each sample, M_s was measured by acquiring an out-of-plane hysteresis loop signal using a vibrating sample magnetometer and then subtracting the linear diamagnetic Si substrate background signal [Fig. 1(b)]. Polar magneto-optical Kerr effect (MOKE) hysteresis loops were taken on samples with perpendicular magnetic anisotropy using a 660-nm laser. In the visible regime, the Kerr rotation is dominated by the Co sublattice, allowing one to determine the magnetically dominant sublattice via the polarity of a MOKE loop [13]. Measured MOKE loops for 6-nm GdCo are shown in Fig. 1(c). The polarity change from $x = 0.25$ to 0.35 indicates the samples shifting from Co to Gd dominated with increasing Gd content.

Figures 1(d) and 1(e) show measured and previously reported M_s values for GdCo and TbCo films as a function of RE content at room temperature. The precise thickness of the GdCo measured in Ref. [14] [Fig. 1(d), black squares] was not reported; however, based on the stated deposition rate (50 nm/min) and thickness of the protective capping layer (30–100 nm), we conclude the thickness to be at least 100 nm. The node position of the solid curves, indicating the magnetic compensation composition, was verified by confirming a polarity change in the MOKE hysteresis loops for

the grown films (6 nm and below). In both GdCo and TbCo films, the magnetic compensation composition of thick films is $x \approx 0.22$. As t decreases, the compensation composition shifts to higher x , shifting to $x \approx 0.3$ for 6-nm films and $x \approx 0.52$ for 3-nm films.

Proximity-induced magnetism (PIM) can exist at Pt/Co interfaces and could in principle cause the apparent magnetic compensation point to shift. An unaccounted-for magnetic Pt layer would lead to an overestimation (underestimation) of the measured RE-Co M_s ($M_{s,\text{meas}}$) if it were oriented parallel (antiparallel) to the net magnetization. This effect can be quantified as

$$\frac{M_{s,\text{meas}}}{M_{s,\text{RE-Co}}} = 1 + \frac{M_{s,\text{Pt}}t_{\text{Pt}}}{M_{s,\text{RE-Co}}t}, \quad (1)$$

where $M_{s,\text{RE-Co}}$ and $M_{s,\text{Pt}}$ are the true M_s of RE-Co and Pt, respectively, $M_{s,\text{Pt}}t_{\text{Pt}}$ is the areal moment density of the magnetic Pt, and the rightmost term quantifies the fractional overestimate. Given the previously reported effective proximity moment of $\sim 1 \mu_B$ per interfacial Pt atom [15], we calculate $M_{s,\text{Pt}}t_{\text{Pt}} = 130 \mu\text{A}$, which would shift x_{comp} by only ~ 1 at.% RE for $t = 3$ nm. We conclude that PIM cannot account for the ~ 30 at.% Gd shift in x_{comp} observed in Fig. 1(d) at low t . Instead, the shift in x_{comp} implies a decrease in the ratio of the effective RE magnetic moment relative to the Co magnetic moment with decreasing t .

To quantify the sublattice magnetic moments, we conducted XMCD measurements on 6-nm GdCo and TbCo composition series at 2 and 300 K. Previous studies have used XMCD to probe the magnetic properties of each

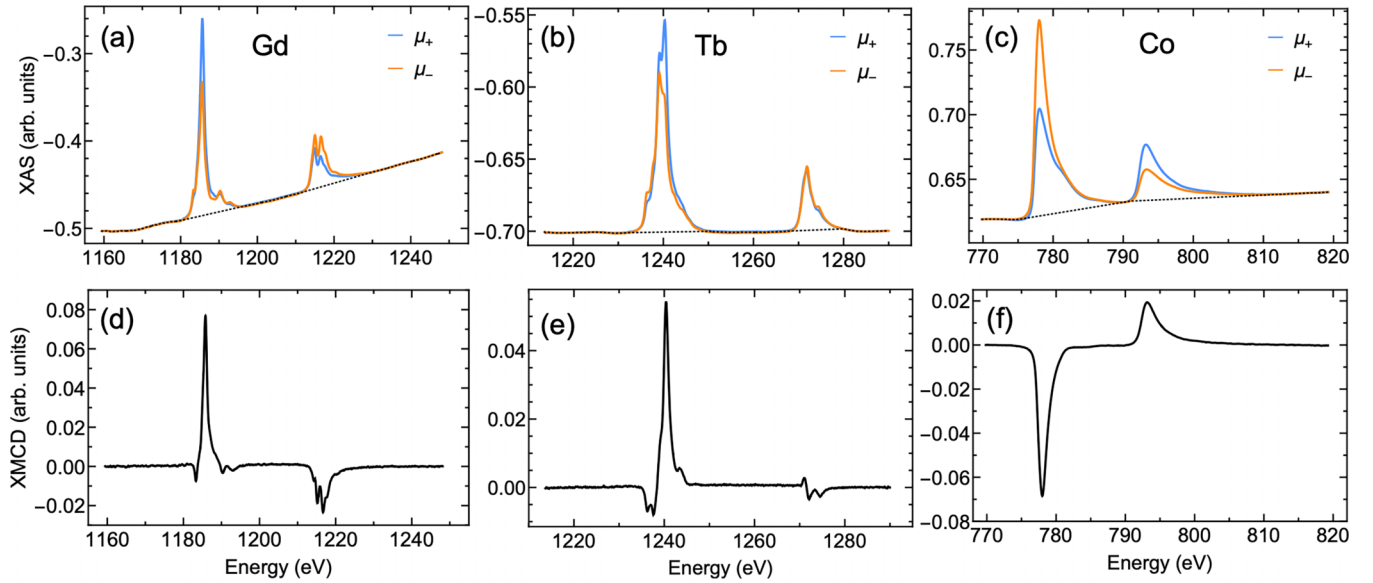


FIG. 2. Representative x-ray absorption spectroscopy (XAS) and x-ray magnetic circular dichroism (XMCD) spectra of perpendicularly saturated 6-nm GdCo and TbCo. Top plots (a)–(c): X-ray absorption spectra at Gd $M_{5,4}$, Tb $M_{5,4}$, and Co $L_{3,2}$ edges using positive (μ_+ , blue) and negative (μ_- , orange) circularly polarized light. Black dotted line is interpolated background function used for calculation of r (see text). Bottom plots (d)–(f): XMCD signal derived from $\mu_+ - \mu_-$. Spectra (a), (c), (d), and (f) are of 6-nm Gd_{0.25}Co_{0.75}. Spectra (b) and (e) are of 6-nm Tb_{0.28}Co_{0.72}.

sublattice in RE-TM films [16–23]; however, a comprehensive study of sublattice magnetic moments over a wide range of compositions has yet to be reported. X-ray absorption spectroscopy (XAS) measurements were taken in a transmission geometry at the BOREAS beamline of the ALBA synchrotron using a 90% circularly polarized x-ray beam produced by an Apple-II-type undulator. The incident beam was normalized using a gold mesh. A field of 15 kOe was selected to ensure sample saturation. Four spectra were collected at each helicity at the Gd or Tb $M_{5,4}$ and Co $L_{3,2}$ edges. The XAS spectra of each element were aligned to have consistent pre-edge and postedge intensities, and the best-fit line of the pre-edge and postedge regions was subtracted from the raw spectra to yield the corrected XAS spectra in Figs. 2(a)–2(c). The XMCD signal was then calculated from the difference of the aligned XAS spectra at each helicity [Figs. 2(d)–2(f)]. The remaining XAS background was removed for determination of r by subtracting the linear interpolation of off-peak intervals from the raw spectra for each helicity. The off-peak intervals for interpolation were defined as $E < 1180$ eV, 1196 eV $< E < 1210$ eV, and $E > 1230$ eV for Gd; $E < 1232$ eV, 1250 eV $< E < 1268$ eV, and $E > 1280$ eV for Tb; and $E < 775$ eV, 790 eV $< E < 790.8$ eV, and $E > 815$ eV for Co. The background functions are plotted in Figs. 2(a)–2(c).

The averaged orbital (m_o) and spin (m_s) atomic magnetic moments of the RE elements were calculated using the relations [24,25]:

$$m_z = m_o + m_s, \quad m_{o,RE} = -\frac{2q}{r}N_h\mu_B, \quad m_{s,RE} = -2\frac{\langle S_{\text{eff}} \rangle}{2 + 6\frac{\langle T_z \rangle_{\text{free}}}{\langle S_z \rangle_{\text{free}}}}\mu_B, \quad \langle S_{\text{eff}} \rangle = \frac{5p - 3q}{r}N_h, \quad (2)$$

with the free ion dipolar and spin operators $\langle T_z \rangle_{\text{free}} = 0.010$ and $\langle S_z \rangle_{\text{free}} = -3.466$ for Gd, and $\langle T_z \rangle_{\text{free}} = 0.243$ and $\langle S_z \rangle_{\text{free}} = -2.943$ for Tb, respectively [26]. The number of holes $N_h = 7$ and 6 were chosen for Gd and Tb, respectively [16]. Similar relations were used for the Co sublattice [24,27]:

$$m_{o,Co} = -\frac{4q}{3r}N_h\mu_B, \quad m_{s,Co} = -\frac{6p - 4q}{r}N_h\mu_B, \quad (3)$$

with $N_h = 2.5$ for Co [16]. The integrated values of the XMCD and background-corrected XAS spectra were used to determine $p = \int_{L_3/M_5}(\mu_+ - \mu_-)d\omega$, $q = \int_{L_3+L_2/M_5+M_4}(\mu_+ - \mu_-)d\omega$, and $r = \int_{L_3+L_2/M_5+M_4}(\mu_+ + \mu_-)d\omega$.

III. RESULTS AND DISCUSSION

The extracted atomic magnetic moment magnitudes of 6-nm GdCo and TbCo as a function of composition are plotted in Fig. 3. In both GdCo and TbCo, the RE and Co moments have opposite signs across all compositions, indicating persistent antiferromagnetic ordering, consistent with previous observations of ferrimagnetic order in GdCo films as thin as 1 nm [16]. In the GdCo series, the orientations of the two sublattices invert between $x = 0.25$ and 0.3 , suggesting a magnetic compensation composition in this range, consistent with the node of the red solid line in Fig. 1(d) and considerably higher than previously reported values in thick films of around $x = 0.2$ – 0.22 [13,14]. The Tb and Co sublattice orientations invert between $x = 0.31$ and 0.36 , similarly far from the magnetization compensation composition found in 100-nm films [28].

As seen in Figs. 3(a)–3(d), the magnitudes of the Gd, Tb, and Co moments decrease monotonically with increasing x at compositions above $x \approx 0.2$. The fact that the Co moment approaches the bulk moment of $\sim 1.7 \mu_B$ as $x \rightarrow 0$ suggests

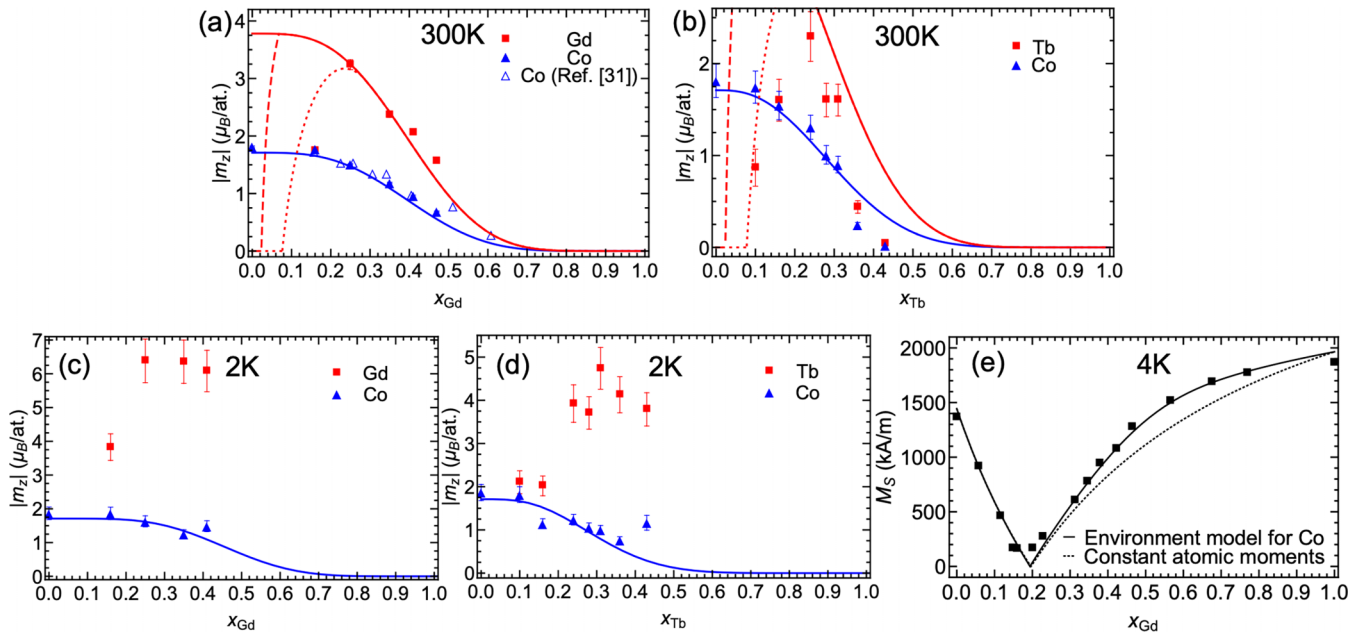


FIG. 3. Average atomic moment variation of 6-nm (a) GdCo and (b) TbCo with varying rare-earth (RE) composition at (a) and (b) 300 K and (c) and (d) 2 K. (a) and (b) Average atomic magnetic moments at 300 K. The combined environment and RE dead layer model is indicated by the solid red and blue lines with (a) $j = 7$ and (b) $j = 10$. The dashed (dotted) red lines indicate the predicted moment variation due to preferential deposition of one (three) atomic layer(s) of dead RE prior to alloy formation (see text). The open blue triangles in (a) are from a thick film of GdCo in Ref. [31]. (c) and (d) Average atomic magnetic moments at 2 K with (c) $j = 7$ and (d) $j = 9$ for the Co sublattice. (e) GdCo M_s data at 4 K in a thick film, adapted from Ref. [14]. The solid line uses environment model for the Co sublattice, while the dotted line assumes constant moments for both sublattices (see text).

the absence of a significant Co dead layer, as is sometimes observed at interfaces in thin Co films and alloys [29]. The decrease in the Co moment upon alloying with the RE is reminiscent of previous studies of magnetic TMs (Fe, Co, and Ni) alloyed with nonmagnetic impurities, which report a similar decrease in TM moment with increasing impurity concentration [30,31]. The reduction in TM moment has been accurately described by a discontinuous environment model proposed by Jacarino and Walker [30]. This model asserts that the magnetic moment of a given magnetic TM atom is either zero or a maximum, depending on the number of TM atoms surrounding it. The average atomic moment is then just the maximum moment multiplied by the probability of a given atom having at least a critical number of TM-atom nearest neighbors. Described mathematically in the context of RE-Co, the average atomic moment of species i (Co, Gd, or Tb) is

$$m_{z,i,env}(x) = P_j(x)m_{z,i}(x=0), \quad (4)$$

where x is the RE atomic fraction, and

$$P_j(x) = \sum_{k=j}^N \binom{N}{k} (1-x)^k x^{N-k} \quad (5)$$

is the probability of an atom having at least j nearest-neighbor Co atoms as a function of RE concentration. Here, N is the coordination number, $m_{z,i}(x=0)$ is the maximum magnetic moment of species i , which occurs at $x=0$, and $\binom{N}{k} = \frac{N!}{(N-k)!k!}$ is the binomial coefficient. Amorphous GdCo and

TbCo have a random dense-packed structure with maximal coordination numbers of $N = 12$ [31,32].

The solid blue lines in Fig. 3 show the environment model applied to the Co sublattice $m_{z,Co}(x=0) = 1.71 \mu_B$, showing excellent agreement with the measured Co moments in both GdCo and TbCo (solid blue triangles) at both 300 and 2 K. The critical number of nearest Co neighbors j is found to be 7 for GdCo [Fig. 3(a)] and 10 for TbCo [Fig. 3(b)] at room temperature. Previous investigations into atomic moment variations in magnetic alloys have focused on TM atomic moments and have found critical j values ranging from 4 in $\text{LaCo}_{5x}\text{Cu}_{5-5x}$ to 8 in $\text{Y}_x\text{Co}_{1-x}$ alloys [30,31]. Replacing Y with Gd reduces the necessary number of nearest neighbors to 7, potentially arising from the influence of the weak Gd-Co antiferromagnetic interaction in addition to the strong Co-Co interaction. The open triangles in Fig. 3(a) correspond to data taken from Ref. [31] for Co in thick GdCo films. The consistency between the Co moments in thick and thin films suggests the Co magnetic moment is independent of film thickness. XMCD measurements performed by Streubel *et al.* [16] on 1–15-nm GdCo confirm this assertion.

The RE atomic moment in RE-TM alloys is often assumed to remain constant across all compositions [33–36]. In contrast, our XMCD results at 300 K reveal nonlinear RE moment dependencies on composition in both GdCo [Fig. 3(a)] and TbCo [Fig. 3(b)]. Both Gd and Tb have Curie temperatures < 300 K [37], which suggests that the Gd-Gd/Tb-Tb interactions are negligibly weak relative to the Gd-Co/Tb-Co interactions. As a result, the RE atoms are highly sensitive

to the local Co environment at temperatures near and above the RE Curie temperature T_c . The solid red lines in Figs. 3(a) and 3(b) show the environment model applied to the Gd (Tb) moments with $j = 7$ ($j = 10$) and $m_{z,\text{Gd}}(x = 0) = 3.25 \mu_B$ [$m_{z,\text{Tb}}(x = 0) = 4.5 \mu_B$]. Above $x = 0.2$, the environment model reasonably predicts the average RE atomic moment, especially for Gd. At low RE concentrations, both Gd and Tb moments are significantly lower than the environment model predicts. We speculate that this moment reduction may be caused by the preferential growth of a RE dead layer at the Pt/RE-Co interface. This is discussed further below.

Upon reducing T to 2 K [Figs. 3(c) and 3(d)], the Co moments are virtually unchanged. The RE moments, however, are approximately constant above $x = 0.2$, suggesting that the environment model is still valid at low temperatures for TMs but not for REs, as the RE-RE interactions become dominant relative to the RE-TM interactions. The low-temperature RE moments allow us to determine the maximum possible fraction of Gd and Tb lost to oxidation during the deposition process by comparing our measured values with previous studies on pure Gd and Tb at low temperatures. Taking the 0-K atomic Gd moment as $7.02 \mu_B$ [26] or $7.63 \mu_B$ [38] and the measured Gd moment averaged over the films with x_{Gd} spanning 0.2–0.45 as $\sim 6.3 \pm 0.4 \mu_B$, we determine a maximum Gd oxidation of $11 \pm 5\%$ or $18 \pm 5\%$ during deposition. A similar calculation on the Tb moments using $9.34 \mu_B$ as the 0-K Tb moment [39] yields a Tb moment of $4.1 \pm 0.2 \mu_B$, corresponding to a maximum Tb oxidation of $57 \pm 2\%$. We note that, although the XAS spectra contain chemical state information, in our case, they do not allow us to unambiguously characterize possible oxidation of the RE in our structures. The RE edges are unaffected by oxidation and the O K edge cannot be used to discriminate between oxidized RE elements and Ta oxide, which is present due to partial oxidation of the capping layer.

Nonetheless, our data suggest that the highly reduced 2-K Tb moment is likely due to a combination of oxidation during deposition and the sperimagnetic character of TbCo. Higher Tb oxidation is expected due to a vacuum break between deposition of Ta/Pt/TbCo/Ta and the protective Ta/Pt capping layer because of a sputter gun limitation. Without a vacuum break, we expect the Tb to oxidize at a similarly low rate as the Gd. Additionally, in TbCo, the RE and Co sublattices are not collinear in contrast to GdCo, with Tb cone angles $>150^\circ$ reported [17,32,40,41]. As a result, the average Tb moment projected along the film normal will be reduced relative to elemental Tb.

Low-temperature M_s data of thick GdCo films as a function of Gd content are consistent with our finding of constant RE and decreasing TM moment with increasing Gd concentration at low T . Figure 3(e) shows M_s for thick GdCo films at 4 K, taken from the report of Hansen *et al.* [14]. The dotted line shows the predicted saturation magnetization assuming both the RE and Co moments do not change with composition:

$$M_s(x) = \left| \frac{m_{z,\text{Co}}(1-x) - m_{z,\text{RE}}x}{v_{\text{Co}}(1-x) + v_{\text{RE}}x} \right|, \quad (6)$$

with $m_{z,\text{Co}} = 1.72 \mu_B$, consistent with previous low-temperature moment measurements [27,42], and $m_{z,\text{Gd}} = 7 \mu_B$. Here, $v_{\text{Co}} = 1.100 \times 10^{-29} \text{ m}^3$, $v_{\text{Gd}} = 3.305 \times 10^{-29} \text{ m}^3$, and $v_{\text{Tb}} = 3.211 \times 10^{-29} \text{ m}^3$ are the atomic volumes of Co, Gd, and Tb derived from their bulk densities. This constant moment model predicts M_s well below compensation but underestimates the observed magnetizations at higher Gd concentrations. The solid curve in Fig. 3(e) instead assumes that the Co moment decreases according to the environment model with $j = 7$ [$m_{z,\text{Co}}(x) = 1.72 \mu_B P_7(x)$] but keeps the Gd moment constant, as indicated by the XMCD results. The resulting curve overlaps the constant moment curve below compensation but predicts higher magnetizations above compensation in alignment with the data. We conclude that far below T_c of the RE, while the TM moment still decreases with increasing RE concentration, as it does at room temperature, the RE moment is no longer affected by its local environment, maintaining a constant moment independent of composition.

Having determined the GdCo atomic moment variations with composition, we investigated the apparent shift in compensation composition with decreasing ferrimagnet thickness. We first measured $M_s(T)$ for a 3-nm $\text{Gd}_{0.7}\text{Co}_{0.3}$ film, which had the highest Gd concentration in our film series, using superconducting quantum interference device (SQUID) magnetometry. The results are shown in Fig. 4(a). Previous work has found that T_c is reduced to below room temperature for Gd concentrations above $x \approx 0.47$ in thick films [Fig. 1(d)] where, for example, $T_c \sim 200$ K for $x = 0.7$ [13,14]. We observe a significant saturation magnetization of 135 kA/m at 300 K in our 3-nm $\text{Gd}_{0.7}\text{Co}_{0.3}$ film, in stark contrast with that finding. The low-temperature M_s value of 1660 kA/m in Ref. [14], however, agrees well with the 4-K data in Fig. 3(e), indicating the nominal composition is accurate. The concavity of the plot in Fig. 4(a) is also notable. The T dependence of RE-TM alloys can typically be approximated by two sublattices following a power law with critical exponents, resulting in concave $M_s(T)$ curves except in the linear regime just around compensation [11,22,43]. The 3-nm $\text{Gd}_{0.7}\text{Co}_{0.3}$ film, however, has a convex $M_s(T)$ curve and a sharp drop in M_s from 2 to 100 K. A previous report on TbCo films with $x > 0.7$ and $t < 12$ nm has shown similar $M_s(T)$ behavior [40]. This suggests that there is a third contribution to the total M_s in thin films that has a much stronger temperature dependence than the other two sublattices.

To further confirm the observed M_s thickness dependencies in Fig. 1(d), we grew a thickness series of $\text{Gd}_{0.3}\text{Co}_{0.7}$ films at a constant composition and measured the resulting M_s [Fig. 4(b)]. We observe a striking M_s behavior. At thicknesses >7 nm, M_s is approximately constant, as expected. Below 7 nm, M_s dramatically drops to compensation at 4 nm, then increases again at $t = 3$ nm. The MOKE hysteresis loops undergo a polarity change across the M_s node as well, indicating a switch in dominant sublattice from Gd dominant >4 nm to Co dominant below. The thick film M_s data indicate that $\text{Gd}_{0.3}\text{Co}_{0.7}$ is expected to lie on the Gd-dominated side of compensation, making the 3-nm point anomalous. The crossover to Co dominance at 3 nm could be explained by the reduction in Gd concentration in the alloyed 3-nm GdCo

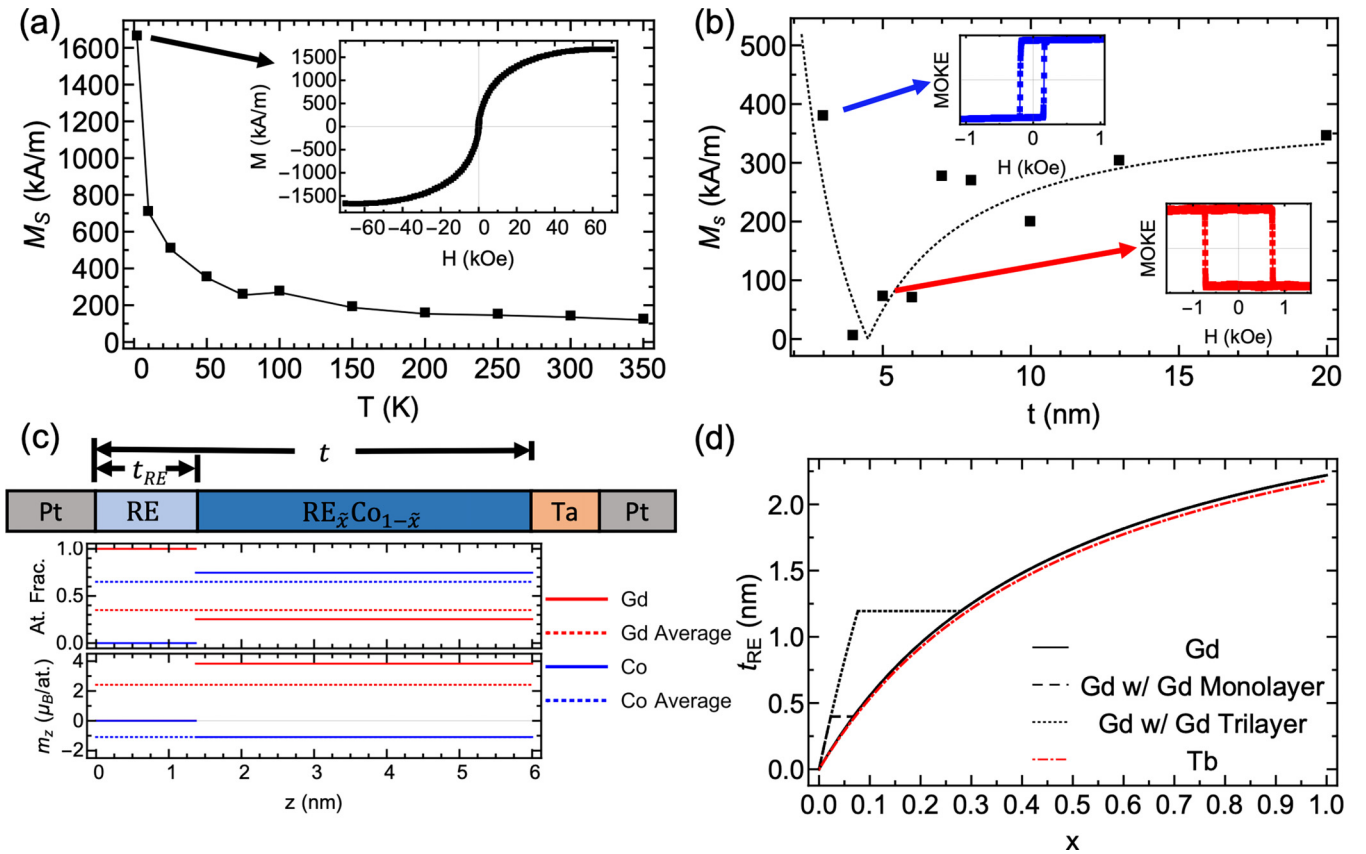


FIG. 4. Dead layer effects on M_s and model schematic. (a) M_s extracted from superconducting quantum interference device (SQUID) hysteresis loops for a 3-nm $\text{Gd}_{0.7}\text{Co}_{0.3}$ film. All loops were measured in an out-of-plane configuration. Inset: 2 K hysteresis loop. (b) M_s data measured at $T = 300$ K for $\text{Gd}_{0.3}\text{Co}_{0.7}$ thickness series. The dotted line is a model prediction for $x_{\text{Gd}} = 0.35$. Insets: Magneto-optical Kerr effect (MOKE) loops indicating Co-dominant (blue) sample at 3 nm and Gd-dominant (red) sample at thicknesses >4 nm. (c) Top: Schematic of rare-earth (RE)-Co sample with RE dead layer and alloyed RE-Co indicated. Middle: Atomic concentration of Gd and Co vs the z coordinate along the film thickness direction. Bottom: Atomic magnetic moment vs the z coordinate. Solid lines indicate the local concentration/moment, while dotted lines indicate the average concentration/moment (equivalent to the nominal concentration) throughout the sample. (d) Best-fit RE dead layer thicknesses used by the model vs RE atomic fraction x .

which would necessarily occur if there was Gd segregation in the sample.

The shift in compensation composition with thickness, the steep, concave reduction in M_s with temperature, and the M_s nodal behavior of the constant composition GdCo thickness series all suggest the presence of paramagnetic, dead Gd at room temperature that is segregated from the alloyed GdCo and only becomes significant in thin films. Previous investigations have observed complex structures in RE-TM alloys such as gradients [44] and agglomerations [45] that could result in a nonmagnetic fraction of RE above and beyond what is predicted by the environment model. Additionally, the Gd atomic moment magnitude has been found to decrease with decreasing film thickness, while the Co moment remains unchanged [16]. For simplicity, we will treat the excess dead Gd as a dead layer to explain our data phenomenologically. The dead layer results in an effective decrease in Gd moment relative to Co moment, resulting in an increase in Gd concentration at compensation with decreasing film thickness seen in Figs. 1(d) and 1(e). The Gd dead layer magnetization decreases faster with increasing T than alloyed Gd since the

dead layer Gd-Gd interactions are far weaker than the alloyed Gd-Co interactions. In very thin films with high Gd content, the Gd dead layer contributes heavily to the overall M_s at low T , resulting in the convex curvature seen in Fig. 4(a). Finally, the presence of a dead layer effectively reduces the concentration of alloyed Gd, whose influence on M_s becomes increasingly important as the ferrimagnetic layer gets thinner. At a critical thickness, this results in a dip in alloyed Gd concentration below the thick film compensation composition and shifts the dominant sublattice from Gd to Co dominant, as seen in Fig. 4(b).

With knowledge of the atomic moment variations with composition and the existence of a RE dead layer, we can model the room-temperature magnetic properties as a function of composition and thickness. To start, we assume a one-dimensional layer structure with an added dead RE layer at the bottom interface of the RE-Co [Fig. 4(c), top], although the physical location of the dead layer is not important to the model. The presence of the pure RE dead layer reduces the RE concentration in the alloyed region below the overall RE composition x to a new composition \bar{x} [Fig. 4(c), middle]. The

atomic concentrations of RE and Co are given by

$$c_{\text{RE}}(x, z) = \begin{cases} 1, & 0 \leq z \leq t_{\text{RE}} \\ \tilde{x}, & t_{\text{RE}} < z \leq t' \end{cases}$$

$$c_{\text{Co}}(x, z) = \begin{cases} 0, & 0 \leq z \leq t_{\text{RE}} \\ 1 - \tilde{x}, & t_{\text{RE}} < z \leq t' \end{cases} \quad (7)$$

$$\tilde{x} = \frac{(t - t_{\text{RE}})xv_{\text{RE}} - t_{\text{RE}}(1 - x)v_{\text{Co}}}{(t - t_{\text{RE}}x)v_{\text{RE}} - t_{\text{RE}}(1 - x)v_{\text{Co}}}, \quad (8)$$

with \tilde{x} derived using the relation (see Appendix):

$$\frac{1}{t} \int_0^t \frac{c_{\text{RE}}v_{\text{RE}}}{c_{\text{RE}}v_{\text{RE}} + (1 - c_{\text{RE}})v_{\text{Co}}} dz = \frac{xv_{\text{RE}}}{xv_{\text{RE}} + (1 - x)v_{\text{Co}}}, \quad (9)$$

given by conservation of volume. The moments are then determined as a function of position z by applying Eq. (4) to the concentration profiles above [Fig. 4(c), bottom]. This results in a reduced average RE moment compared with a thick film due to the influence of the RE dead layer. As a first-order approximation, a constant fraction of RE atoms is assumed to contribute to the RE dead layer, up to a maximum dead layer thickness $t_{\text{RE,max}}$. The resulting dead layer [Fig. 4(d)] is given by $t_{\text{RE,max}}$ scaled by the total RE volume fraction $t_{\text{RE}}(x) = \frac{xv_{\text{RE}}}{xv_{\text{RE}} + (1 - x)v_{\text{Co}}} t_{\text{RE,max}}$. Here, M_s was calculated using Eq. (6) and replacing the average RE moment:

$$\begin{aligned} \bar{m}_{z,\text{RE,env}} &= \frac{(1 - x)\tilde{x}}{x(1 - \tilde{x})} m_{z,\text{RE,env}}[c_{\text{RE}}(x, t_{\text{RE}} < z \leq t)] \\ &= \frac{(1 - x)\tilde{x}}{x(1 - \tilde{x})} m_{z,\text{RE,env}}(\tilde{x}), \end{aligned} \quad (10)$$

for the standard RE moment $m_{z,\text{RE}}$ and using $m_{z,\text{Co,env}}(\tilde{x})$ for $m_{z,\text{Co}}$. This M_s function was then fitted to the $M_s(x)$ data in Figs. 1(d) and 1(e). The critical number of nearest neighbors j and maximum dead layer thickness $t_{\text{RE,max}}$ were chosen as fitting parameters.

The solid curves in Figs. 1(d) and 1(e) show the combined environment and dead layer model fits. The dead layer determines the extent of compensation composition shift with thickness. A single maximum dead layer of $t_{\text{Gd,max}} = 2.22$ nm was found to describe the shift in GdCo compensation composition from the bulk condition in both 6- and 3-nm films. A nearly identical maximum dead layer was found in TbCo [Fig. 4(d)], demonstrating the generalizability of this dead layer model to other RE-TM alloys. The model curves also predict the downturn in M_s observed at high RE concentrations as T_c drops below room temperature. For comparison, the dotted lines in Figs. 1(d) and 1(e) show the calculated M_s under the assumption of constant atomic moments, demonstrating the superior accuracy of the environment model and highlighting the significant errors introduced by ignoring coordination effects.

We return now to the anomalously low RE atomic moments at low RE concentrations seen in Figs. 3(a)–3(d). As previously stated, the RE moments generally follow the environment model except below $x \approx 0.25$. This deviation does not significantly affect the M_s model calculation since the RE concentration is so low that variations in its moment have a minor effect on the volume-averaged M_s . However, it is unusual enough to warrant some speculation. The presence of a dead fraction of RE, whether in the form of a dead layer

or due to agglomerates, implies some form of preferential growth takes place during the deposition of RE and Co upon Pt(111). Both elemental Gd and Tb have a surface energy three times smaller than Co and twice as small as Pt(111) [46]. As such, it is energetically favorable for RE to form an initial monolayer of atoms on Pt(111). This would cause an initially quick buildup of a RE dead monolayer, faster than the constant RE fraction curve assumed in the black solid and red dash-dotted lines in Fig. 4(d), and would result in a reduction in RE moment at low concentrations due to all available RE atoms contributing to the dead layer initially. The dashed and dotted lines in Figs. 3(a) and 3(b) show the calculated moments under the assumption of a preferential Gd or Tb monolayer or trilayer at 300 K, highlighting the reduction in RE moment at low x . Similar reasoning can be applied to the 2-K RE moments. At low T [Figs. 3(c) and 3(d)], one would expect the pure RE layer to be ferromagnetic instead of magnetically dead. As a result, the pure RE moments can either align parallel or antiparallel to the alloyed RE moments, depending on the dominant sublattice in the alloyed region. The anomalously low 2-K RE moments are below $x \approx 0.2$, meaning that the alloyed region is Co dominated. In this case, under an applied field, the Co atoms will align parallel to the field, the alloyed RE atoms will align antiparallel to the field, and the ferromagnetic RE atoms will align parallel to the field, partially cancelling out the alloyed RE moments and resulting in a reduced average RE moment.

In addition to the total atomic moments, XMCD allows for the extraction of orbital and spin moments for each element. Figures 5(a) and 5(b) show the extracted orbital (m_o) and spin (m_s) magnetic moments of 6-nm GdCo and TbCo as a function of RE content at 300 K. As expected, the Gd orbital moment is quite small, whereas the Tb orbital moment is comparable with its spin moment. The atomic spectroscopic g factors were calculated from these moments using the relation [42]: $g = \frac{2m_e}{e} \frac{m_z}{\langle S_z \rangle} = \frac{2(m_s + m_o)}{m_s}$, with m_e the electron mass and $\langle S_z \rangle$ the spin angular momentum. As seen in Figs. 5(c) and 5(d), the atomic g factors vary significantly as a function of composition, with the RE and Co g factors even crossing over each other in both GdCo and TbCo. At the ends of the composition range, the atomic g factors agree with previous measurements ($g_{\text{Gd}} = 2.00$ [47,48], $g_{\text{Co}} = 2.187$ [42]) but deviate from the expected values as their elemental concentration decreases. Elemental g factors are often used to calculate g_{eff} in ferrimagnets [10]. These results indicate that care must be taken to ensure that the atomic g factors do not deviate from their pure elemental values at the composition of interest for accurate computation of net spin properties in RE-TM alloys.

IV. CONCLUSION

RE-TM alloys are an important class of materials for existing and future spintronic devices. Our results show a clear composition and thickness dependence on magnetic properties of the constituent elements in GdCo and TbCo alloys. We find that a nearest-neighbor environment model describes the reduction in both RE and Co moments with increasing RE concentration at room temperature. The presence of a dead RE

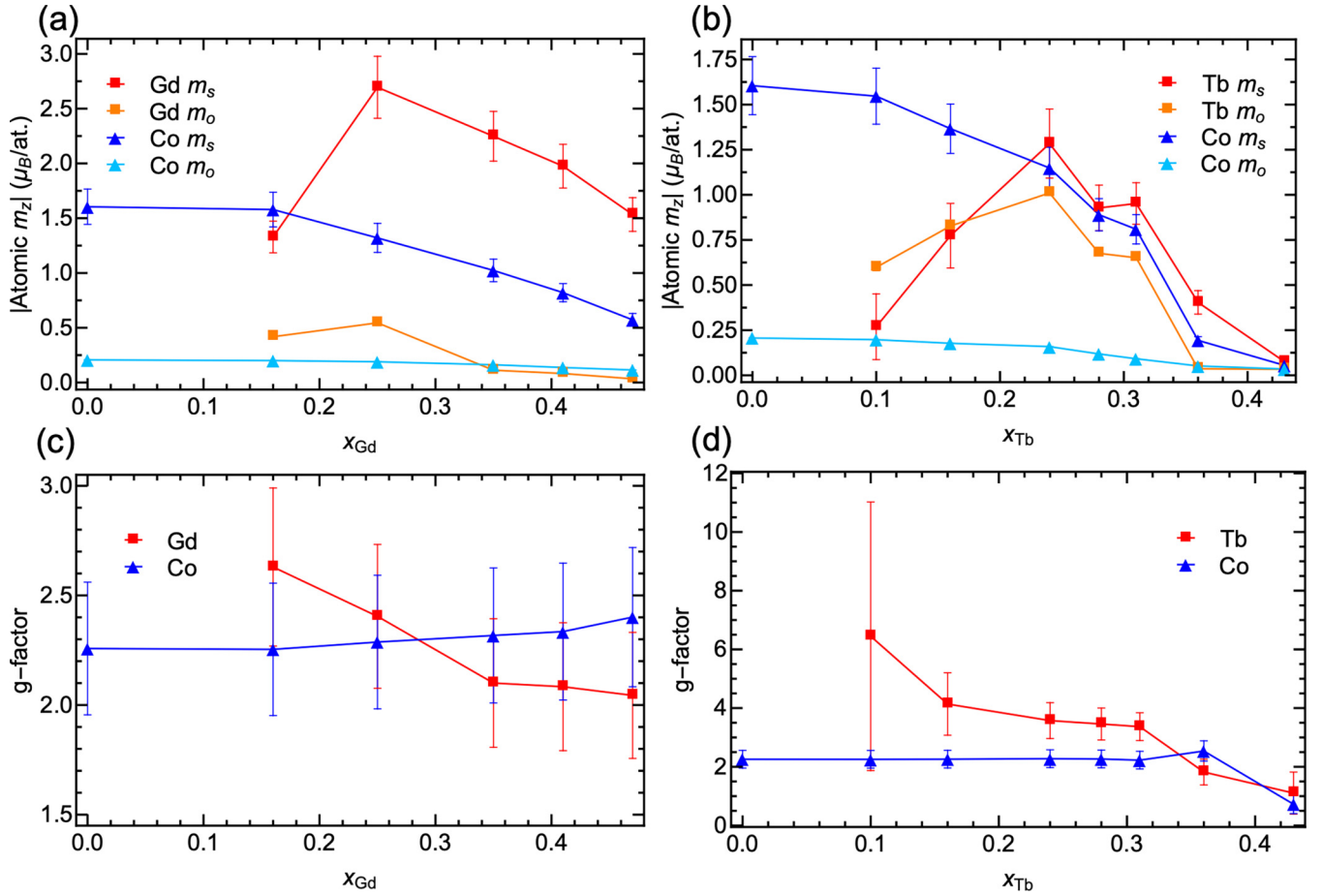


FIG. 5. Spin and orbital moment contributions of GdCo and TbCo at 300 K. (a) GdCo and (b) TbCo spin (m_s) and orbital (m_o) moment data vs rare-earth (RE) atomic fraction derived from x-ray magnetic circular dichroism (XMCD) data. (c) and (d) Atomic spectroscopic g factor data for GdCo and TbCo vs RE atomic fraction, calculated from spin and orbital atomic moments in (a) and (b).

layer results in a systematic shift in magnetic compensation composition as the thickness of the film decreases. We demonstrate a simple, first-order model that predicts the saturation magnetization and average atomic moments as a function of thickness and RE composition. Finally, we observe a significant change in atomic g factors as a function of composition in both GdCo and TbCo. This understanding of fundamental atomic magnetic properties in ferrimagnetic alloys allows future utilization of ultrathin RE-TM films optimized for a variety of spintronic applications.

ACKNOWLEDGMENTS

We acknowledge funding by the Defense Advanced Research Projects Agency Topological Excitations in Electronics Program and Spintronic Materials for Advanced Information Technologies, one of seven centers of nCORE, a Semiconductor Research Corporation program, sponsored by the National Institute of Standards and Technology and the Massachusetts Institute of Technology International Science and Technology Initiatives. The XMCD experiments were performed at BOREAS beamline at ALBA Synchrotron with the collaboration of ALBA staff. We would like to thank E. Goering and G. Schütz at the Max Planck Institute for Intelligent Systems for support regarding the SQUID measurements.

APPENDIX: DERIVATION OF ALLOYED RE ATOMIC FRACTION WITH RE DEAD LAYER

The overall RE volume fraction in a binary alloy of $\text{RE}_x\text{Co}_{1-x}$ is given by

$$f_{\text{RE}} = \frac{xv_{\text{RE}}}{xv_{\text{RE}} + (1-x)v_{\text{Co}}}. \quad (\text{A1})$$

By conservation of volume, this is equal to the RE volume fraction at z averaged over the film thickness, giving Eq. (9). Applying the piecewise concentration profile of the RE from Eq. (7), $c_{\text{RE}}(x, z)$, Eq. (9) expands to

$$\begin{aligned} & \frac{1}{t} \left[\int_0^{t_{\text{RE}}} dz + \int_{t_{\text{RE}}}^t \frac{\tilde{x}v_{\text{RE}}}{\tilde{x}v_{\text{RE}} + (1-\tilde{x})v_{\text{Co}}} dz \right] \\ &= \frac{1}{t} \left[t_{\text{RE}} + (t - t_{\text{RE}}) \frac{\tilde{x}v_{\text{RE}}}{\tilde{x}v_{\text{RE}} + (1-\tilde{x})v_{\text{Co}}} \right] = f_{\text{RE}}. \quad (\text{A2}) \end{aligned}$$

Applying Eq. (A1) to Eq. (A2) and solving for \tilde{x} yields the expression for alloyed RE atomic fraction presented in Eq. (8).

- [1] W. H. Li, Z. Jin, D. L. Wen, X. M. Zhang, M. H. Qin, and J.-M. Liu, Ultrafast domain wall motion in ferrimagnets induced by magnetic anisotropy gradient, *Phys. Rev. B* **101**, 024414 (2020).
- [2] L. Caretta, M. Mann, F. Büttner, K. Ueda, B. Pfau, C. Günther, P. Helsing, A. Churikova, C. Klose, M. Schneider *et al.*, Fast current-driven domain walls and small skyrmions in a compensated ferrimagnet, *Nat. Nanotechnol.* **13**, 1154 (2018).
- [3] S. A. Siddiqui, J. Han, J. T. Finley, C. A. Ross, and L. Liu, Current-Induced Domain Wall Motion in a Compensated Ferrimagnet, *Phys. Rev. Lett.* **121**, 057701 (2018).
- [4] K.-J. Kim, S. K. Kim, Y. Hirata, S.-H. Oh, T. Tono, D.-H. Kim, T. Okuno, W. S. Ham, S. Kim, G. Go *et al.*, Fast domain wall motion in the vicinity of the angular momentum compensation temperature of ferrimagnets, *Nat. Mater.* **16**, 1187 (2017).
- [5] I. Lemesch, K. Litzius, M. Böttcher, P. Bassirian, N. Kerber, D. Heinze, J. Zázvorka, F. Büttner, L. Caretta, M. Mann *et al.*, Current-induced skyrmion generation through morphological thermal transitions in chiral ferromagnetic heterostructures, *Adv. Mater.* **30**, 1805461 (2018).
- [6] S. Mangin, M. Gottwald, C. Lambert, D. Steil, V. Uhlíř, L. Pang, M. Hehn, S. Alebrand, M. Cinchetti, C. Malinowski *et al.*, Engineered materials for all-optical helicity-dependent magnetic switching, *Nat. Mater.* **13**, 286 (2014).
- [7] B. Hebler, A. Hassdenteufel, P. Reinhardt, H. Karl, and M. Albrecht, Ferrimagnetic Tb-Fe alloy thin films: Composition and thickness dependence of magnetic properties and all-optical switching, *Front Mater* **3**, 8 (2016).
- [8] Z. Zheng, Y. Zhang, V. Lopez-Dominguez, L. Sánchez-Tejerina, J. Shi, X. Feng, L. Chen, Z. Wang, Z. Zhang, K. Zhang *et al.*, Field-free spin-orbit torque-induced switching of perpendicular magnetization in a ferrimagnetic layer with a vertical composition gradient, *Nat. Commun.* **12**, 4555 (2021).
- [9] K. Cai, Z. Zhu, J. M. Lee, R. Mishra, L. Ren, S. D. Pollard, P. He, G. Liang, K. L. Teo, and H. Yang, Ultrafast and energy-efficient spin-orbit torque switching in compensated ferrimagnets, *Nat. Electron.* **3**, 37 (2020).
- [10] R. K. Wangsness, Sublattice effects in magnetic resonance, *Phys. Rev.* **91**, 1085 (1953).
- [11] Y. Hirata, D.-H. Kim, T. Okuno, T. Nishimura, D.-Y. Kim, Y. Futakawa, H. Yoshikawa, A. Tsukamoto, K.-J. Kim, S.-B. Choe *et al.*, Correlation between compensation temperatures of magnetization and angular momentum in GdFeCo ferrimagnets, *Phys. Rev. B* **97**, 220403(R) (2018).
- [12] S. Emori, U. Bauer, S. M. Ahn, E. Martinez, and G. S. D. Beach, Current-driven dynamics of chiral ferromagnetic domain walls, *Nat. Mater.* **12**, 611 (2013).
- [13] P. Hansen and H. Heitmann, Media for erasable magneto-optical recording, *IEEE Trans. Magn.* **25**, 4390 (1989).
- [14] P. Hansen, C. Clausen, G. Much, M. Rosenkranz, and K. Witter, Magnetic and magneto-optical properties of rare-earth transition-metal alloys containing Gd, Tb, Fe, Co, *J. Appl. Phys.* **66**, 756 (1989).
- [15] M. Suzuki, H. Muraoka, Y. Inaba, H. Miyagawa, N. Kawamura, T. Shimatsu, H. Maruyama, N. Ishimatsu, Y. Isohama, and Y. Sonobe, Depth profile of spin and orbital magnetic moments in a subnanometer Pt film on Co, *Phys. Rev. B* **72**, 054430 (2005).
- [16] R. Streubel, C. Lambert, N. Kent, P. Ercius, A. T. N'Diaye, C. Ophus, S. Salahuddin, and P. Fischer, Experimental evidence of chiral ferrimagnetism in amorphous GdCo films, *Adv. Mater.* **30**, 1800199 (2018).
- [17] M.-S. Lin, H.-C. Hou, Y.-C. Wu, P.-H. Huang, C.-H. Lai, H.-H. Lin, H.-J. Lin, and F.-H. Chang, Effects of perpendicular interlayer coupling strength on canting angles of TbCo-sublattice magnetization, *Phys. Rev. B* **79**, 140412(R) (2009).
- [18] T. Ueno, N. Inami, R. Sagayama, Z. Wen, M. Hayashi, S. Mitani, R. Kumai, and K. Ono, Relation between electronic structure and magnetic anisotropy in amorphous TbCo films probed by x-ray magnetic circular dichroism, *J. Phys. D: Appl. Phys.* **49**, 205001 (2016).
- [19] M. Huang, M. Hasan, K. Klyukin, D. Zhang, D. Lyu, P. Gargiani, M. Valvidares, S. Sheffels, A. Churikova, F. Büttner *et al.*, Voltage control of ferrimagnetic order and voltage-assisted writing of ferrimagnetic spin textures, *Nat. Nanotechnol.* **16**, 981 (2021).
- [20] N. Berggaard, A. Mougin, M. Izquierdo, E. Fonda, and F. Sirotti, Correlation between structure, electronic properties, and magnetism in $\text{Co}_x\text{Gd}_{1-x}$ thin amorphous films, *Phys. Rev. B* **96**, 064418 (2017).
- [21] R. Cid, J. M. Alameda, S. M. Valvidares, J. C. Cezar, P. Bencok, N. B. Brookes, and J. Díaz, Perpendicular magnetic anisotropy in amorphous $\text{Nd}_x\text{Co}_{1-x}$ thin films studied by x-ray magnetic circular dichroism, *Phys. Rev. B* **95**, 224402 (2017).
- [22] T. A. Ostler, R. F. L. Evans, R. W. Chantrell, U. Atxitia, O. Chubykalo-Fesenko, I. Radu, R. Abrudan, F. Radu, A. Tsukamoto, A. Itoh *et al.*, Crystallographically amorphous ferrimagnetic alloys: Comparing a localized atomistic spin model with experiments, *Phys. Rev. B* **84**, 024407 (2011).
- [23] I. Radu, K. Vahaplar, C. Stamm, T. Kachel, N. Pontius, H. A. Dürr, T. A. Ostler, J. Barker, R. F. L. Evans, R. W. Chantrell *et al.*, Transient ferromagnetic-like state mediating ultrafast reversal of antiferromagnetically coupled spins, *Nature (London)* **472**, 205 (2011).
- [24] H. B. Vasili, B. Casals, R. Cicheler, F. Macià, J. Geshev, P. Gargiani, M. Valvidares, J. Herrero-Martin, E. Pellegrin, J. Fontcuberta *et al.*, Direct observation of multivalent states and $4f \rightarrow 3d$ charge transfer in Ce-doped yttrium iron garnet thin films, *Phys. Rev. B* **96**, 014433 (2017).
- [25] A. Singha, R. Baltic, F. Donati, C. Wäckerlin, J. Dreiser, L. Persichetti, S. Stepanow, P. Gambardella, S. Rusponi, and H. Brune, $4f$ occupancy and magnetism of rare-earth atoms adsorbed on metal substrates, *Phys. Rev. B* **96**, 224418 (2017).
- [26] Y. Teramura, A. Tanaka, B. T. Thole, and T. Jo, Effect of coulomb interaction on the x-ray magnetic circular dichroism spin sum rule in rare earths, *J. Phys. Soc. Jpn.* **65**, 3056 (1996).
- [27] C. T. Chen, Y. U. Idzerda, H.-J. Lin, N. V. Smith, G. Meigs, E. Chaban, G. H. Ho, E. Pellegrin, and F. Sette, Experimental Confirmation of the X-Ray Magnetic Circular Dichroism Sum Rules for Iron and Cobalt, *Phys. Rev. Lett.* **75**, 152 (1995).
- [28] Y. J. Choe, S. Tsunashima, T. Katayama, and S. Uchiyama, Magneto-optic Kerr spectra of amorphous RE-Co thin films, *J. Mag. Soc. Jpn.* **11**, S1_273 (1987).
- [29] N. Sato, K. P. O'Brien, K. Millard, B. Doyle, and K. Oguz, Investigation of extrinsic damping caused by magnetic dead layer in Ta-CoFeB-MgO multilayers with perpendicular anisotropy, *J. Appl. Phys.* **119**, 093902 (2016).
- [30] V. Jaccarino and L. R. Walker, Discontinuous Occurrence of Localized Moments in Metals, *Phys. Rev. Lett.* **15**, 258 (1965).

- [31] K. H. J. Buschow, M. Brouha, J. W. M. Biesterbos, and A. G. Dirks, Crystalline and amorphous rare-earth transition metal alloys, *Physica B+C* **91**, 261 (1977).
- [32] J. M. D. Coey, Amorphous magnetic order, *J. Appl. Phys.* **49**, 1646 (1978).
- [33] M. Binder, A. Weber, O. Mosendz, G. Woltersdorf, M. Izquierdo, I. Neudecker, J. R. Dahn, T. D. Hatchard, J.-U. Thiele, C. H. Back *et al.*, Magnetization dynamics of the ferrimagnet CoGd near the compensation of magnetization and angular momentum, *Phys. Rev. B* **74**, 134404 (2006).
- [34] C. T. Ma, Y. Xie, H. Sheng, A. W. Ghosh, and S. J. Poon, Robust formation of ultrasmall room-temperature Néel skyrmions in amorphous ferrimagnets from atomistic simulations, *Sci. Rep.* **9**, 9964 (2019).
- [35] A. V. Svalov, O. A. Adanakova, V. O. Vas'kovskiy, K. G. Balymov, A. Larrañaga, G. V. Kurlyandskaya, R. Domingues Della Pace, and C. C. Plá Cid, Thickness dependence of magnetic properties of thin amorphous ferrimagnetic rare earth–transition metal multilayers, *J. Magn. Magn. Mater.* **459**, 57 (2018).
- [36] M. J. Besnus, A. Herr, and G. Fischer, On the magnetic properties of Gd(Fe_{1-x}Al_x)₂ compounds, *J. Phys. F: Met. Phys.* **9**, 745 (1979).
- [37] W. C. Koehler, Magnetic properties of rare-earth metals and alloys, *J. Appl. Phys.* **36**, 1078 (1965).
- [38] H. W. White, B. J. Beaudry, P. Burgardt, S. Legvold, and B. N. Harmon, Magnetic moments of ferromagnetic gadolinium alloys, *AIP Conf. Proc.* **29**, 329 (1976).
- [39] D. E. Hegland, S. Legvold, and F. H. Spedding, Magnetization and electrical resistivity of terbium single crystals, *Phys. Rev.* **131**, 158 (1963).
- [40] A. V. Svalov, I. A. Makarochkin, E. V. Kudyukov, E. A. Stepanova, V. O. Vas'kovskii, A. Larrañaga, and G. V. Kurlyandskaya, Changes in the magnetic structure upon varying the magnetic layer thickness in [Tb–Co/Si]_n films, *Phys. Met. Metall.* **122**, 115 (2021).
- [41] V. O. Vas'kovskiy, O. A. Adanakova, K. G. Balymov, N. A. Kulesh, A. V. Svalov, and E. A. Stepanova, Specific features of the formation of atomic magnetic moments in amorphous films RE–Co (RE = La, Gd, Tb), *Phys. Solid State* **57**, 1142 (2015).
- [42] B. I. Min and Y.-R. Jang, The effect of the spin-orbit interaction on the electronic structure of magnetic materials, *J. Phys.: Condens. Matter* **3**, 5131 (1991).
- [43] S. Chikazumi, *Physics of Ferromagnetism*, 2nd ed. (Oxford University Press, Oxford, 1997).
- [44] D.-H. Kim, M. Haruta, H.-W. Ko, G. Go, H.-J. Park, T. Nishimura, D.-Y. Kim, T. Okuno, Y. Hirata, Y. Futakawa *et al.*, Bulk Dzyaloshinskii-Moriya interaction in amorphous ferrimagnetic alloys, *Nat. Mater.* **18**, 685 (2019).
- [45] G. Sala, C.-H. Lambert, S. Finizio, V. Raposo, V. Krizakova, G. Krishnaswamy, M. Weigand, J. Raabe, M. Rossell, E. Martinez *et al.*, Asynchronous current-induced switching of rare-earth and transition-metal sublattices in ferrimagnetic alloys, *Nat. Mater.* **21**, 640 (2022).
- [46] R. Tran, Z. Xu, B. Radhakrishnan, D. Winston, W. Sun, K. A. Persson, and S. P. Ong, Surface energies of elemental crystals, *Sci Data* **3**, 160080 (2016).
- [47] J. Sticht and J. Kübler, Electronic structure of ferromagnetic Gd, *Solid State Commun.* **53**, 529 (1985).
- [48] Y. Ogata, H. Chudo, M. Ono, K. Harii, M. Matsuo, S. Maekawa, and E. Saitoh, Gyroscopic *g* factor of rare earth metals, *Appl. Phys. Lett.* **110**, 072409 (2017).